

JET MOTION, INTERNAL WORKING SURFACES, AND NESTED SHELLS IN THE PROTOSTELLAR SYSTEM HH 212

CHIN-FEI LEE¹, NAOMI HIRANO¹, QIZHOU ZHANG², HSIEN SHANG¹, PAUL T. P. HO^{1,2}, AND YOSUKE MIZUNO³

¹ Academia Sinica Institute of Astronomy and Astrophysics, P.O. Box 23-141, Taipei 106, Taiwan; cflee@asiaa.sinica.edu.tw

² Harvard-Smithsonian Center for Astrophysics, 60 Garden Street, Cambridge, MA 02138, USA

³ Institute for Theoretical Physics, Goethe University, Frankfurt am Main, D-60438, Germany

Received 2015 January 28; accepted 2015 March 24; published 2015 June 2

ABSTRACT

HH 212 is a nearby (400 pc) highly collimated protostellar jet powered by a Class 0 source in Orion. We have mapped the inner 80'' (~ 0.16 pc) of the jet in SiO ($J = 8 - 7$) and CO ($J = 3 - 2$) simultaneously at $\sim 0''.5$ resolution with the Atacama Millimeter/Submillimeter Array (SMA) at unprecedented sensitivity. The jet consists of a chain of knots and bow shocks with sinuous structures in between. Compared to what we saw in our previous observations with the SMA, the jet appears to be more continuous, especially in the northern part. Some of the knots are now observed to be associated with small bow shocks, with their bow wings curving back to the jet axis, as seen in pulsed jet simulations. Two of the knots are reasonably resolved, showing kinematics consistent with sideways ejection, possibly tracing the internal working surfaces formed by a temporal variation in the jet velocity. In addition, nested shells are seen in CO around the jet axis connecting to the knots and bow shocks, driven by them. The proper motion of the jet is estimated to be $\sim 115 \pm 50 \text{ km s}^{-1}$, comparing with our previous observations. The jet has a small semi-periodical wiggle with a period of ~ 93 yr. The amplitude of the wiggle first increases with the distance from the central source and then stays roughly constant. One possible origin of the wiggle could be the kink instability in a magnetized jet.

Key words: ISM: individual objects (HH 212) – ISM: jets and outflows – stars: formation

1. INTRODUCTION

Protostellar jets represent one of the most intriguing signposts of star formation (for a recent review see Frank et al. 2014). They are highly supersonic and collimated and some have wiggles in their trajectories. They are seen with knotty and bow-like shock structures. They can be launched from accretion disks around protostars, allowing us to probe the accretion process closest to the protostars. Two competing, yet similar, MHD models, the X-wind model (Shu et al. 2000) and disk-wind model (Konigl & Pudritz 2000), have been proposed to launch these jets. Preliminary measurements of the specific angular momentum of some jets are consistent with these two models (see, e.g., Lee et al. 2008; Coffey et al. 2011). Polarization observations also suggest that the jets could be magnetized (Carrasco-González et al. 2010; Lee et al. 2014b), as predicted in the two models. Therefore, more detailed studies of the jet properties are needed to determine the jet launching model and, thus, the accretion process closest to the protostars.

Molecular outflows are shell-like structures surrounding the jets, and thus can be used to indirectly probe the physical properties of the jets. They are believed to be outflow cavity walls consisting mainly of the ambient material swept up by the bow shocks in the jets (see, e.g., Lee et al. 2001). Since some molecular outflows show wide-opening cavity walls near the protostars, especially in the later stage of star formation (Lee & Ho 2005; Arce et al. 2013), additional unseen wide-angle tenuous winds might be required. Indeed, current theoretical jet models also predict such winds surrounding the highly collimated jets (Konigl & Pudritz 2000; Shu et al. 2000). However, more observations are still needed to confirm this possibility, especially in the early phase of star formation.

This paper is a follow-up study to our previous Submillimeter Array (SMA) study of the HH 212 jet and outflow

system (Lee et al. 2007, 2008); presenting our study in SiO and CO with the Atacama Millimeter/SMA (ALMA) at an angular resolution of $\sim 0''.5$ with more than 10 times higher sensitivity. The HH 212 system is nearby in the L1630 cloud of Orion at a distance of ~ 400 pc. Its jet was discovered in shock-excited H₂ emission (Zinnecker et al. 1998). It is powered by a low-luminosity ($\sim 9 L_{\odot}$) Class 0 protostar IRAS 05413–0104. It interacts with the ambient material, driving a collimated CO outflow around it (Lee et al. 2000). A rotationally supported disk is believed to have formed around the protostar in order to launch the jet (Codella et al. 2014; Lee et al. 2014). Lying close to the plane of the sky ($\lesssim 5^{\circ}$, Claussen et al. 1998; Lee et al. 2007), the jet is one of the best candidates to investigate the jet's properties. Here, we refine the proper motion, and thus the mass-loss rate, of the jet. We study the shock structures in the jet, the morphological relationship between the CO outflow and the jet, and discuss if there is need for a wide-angle tenuous wind around the jet. The jet has a small semi-periodical wiggle. We model the wiggle and discuss its possible origins. Note that the small jet rotation tentatively found at a higher resolution of $\sim 0''.35$ in SiO (Lee et al. 2008) cannot be confirmed here at a lower resolution of $\sim 0''.5$.

2. OBSERVATIONS

Observations of the HH 212 protostellar system were carried out with ALMA on 2012 December 1 during the Early Science Cycle 0 phase. The details of these observations have been reported in Lee et al. (2014), and thus only important information is reported here. A nine-pointing mosaic was used to observe the jet in this system within $\sim 40''$ from the central source. Both CO $J = 3 - 2$ and SiO $J = 8 - 7$ lines were observed at a velocity resolution of $\sim 0.21 \text{ km s}^{-1}$ per channel. With super-uniform weighting, the synthesized beam has a size of $0''.53 \times 0''.47$ at a position angle (PA) of $\sim 20^{\circ}$ in SiO and

$0''.56 \times 0''.47$ at a PA of 43° in CO. The rms noise level is $\sim 7.7 \text{ mJy beam}^{-1}$ (i.e., 0.32 K) for the SiO channel maps and $\sim 7.2 \text{ mJy beam}^{-1}$ (i.e., 0.28 K) for the CO channel maps. The velocities in the channel maps are LSR. The systemic velocity in this region is assumed to be $V_{\text{sys}} = 1.7 \pm 0.1 \text{ km s}^{-1}$ LSR, as in Lee et al. (2007). The central source is assumed to be at the peak position of the continuum, which is $\alpha_{(2000)} = 05^{\text{h}}43^{\text{m}}51^{\text{s}}.4107$, $\delta_{(2000)} = -01^\circ02'53''.167$, as in Lee et al. (2014).

3. RESULTS

In order to provide readers with a more complete picture of the jet and outflow system, our ALMA maps are plotted together with an earlier H_2 map of the jet. Also, for a better view, all the maps are rotated by 22.5° clockwise so that the jet axis is aligned with the y-axis. The H_2 map shows that the jet consists of a chain of knots and bow shocks with sinuous (continuous) structures in between. It was made by combining the three observations in 2000 October, 2001 October, and 2002 January (McCaughrean et al. 2002), and is thus roughly 11 years earlier than our ALMA observations. Since the proper motion of the jet is estimated to be $\sim 0''.06 \text{ yr}^{-1}$ later in this paper, the H_2 jet must have moved down the jet axis by $\sim 0''.7$, as compared to the jet seen in our ALMA maps. Since this position shift is smaller than the size of a knot ($\gtrsim 1''$), the H_2 map can still be used to show the rough positions of the knots, bow shocks, and sinuous structures compared with our ALMA maps.

3.1. Nested Shells in CO

With ALMA, CO emission can now be mapped at higher angular resolution and sensitivity. Figure 1 shows the CO maps from blueshifted to redshifted velocities (with a velocity interval of 4.23 km s^{-1}) compared to the H_2 map. The blueshifted emission is mainly to the north and the redshifted mainly to the south of the central source. Nested shell structures are seen extending to the north and south from the central source. As shown in Figure 2, the nested shell structures can be better seen in the CO maps integrated over selected velocity ranges that show the shell structures. In the south (Figure 2(a)), a wide-opening shell is seen opening to the south of the central source, connecting to the big bow shock SB3 farther out. Likewise in the north (Figure 2(b)), a similar wide-opening shell is seen opening to the north, connecting to the big bow shock NB3 farther out. These wide-opening shells are also seen in the lower transition line of CO at $J = 2 - 1$ (Lee et al. 2006), likely tracing the outflow cavity walls consisting mainly of the ambient material swept up by the big bow shocks. At the base around the central source (see the zoomed-in area in Figure 3(c)), the shells fit right into the bay of the flattened envelope detected in the 350 GHz continuum (Lee et al. 2014). This morphological relationship suggests that as the shells expand they are sweeping up, and thus excavating, the flattened envelope at the base.

Inside these wide-opening shells, internal shells are seen connecting to bow shocks NB1/2 and SB1/2 from the central source (Figure 2). Here, internal shells are referring to the shells located inside the cavity walls (Lee et al. 2001). In the north, the internal shell is also affected by the wings of bow shocks NK7 and NK8 inside the shell (Figures 1(c)–(g)). Inside these shells, CO emission is also seen surrounding other

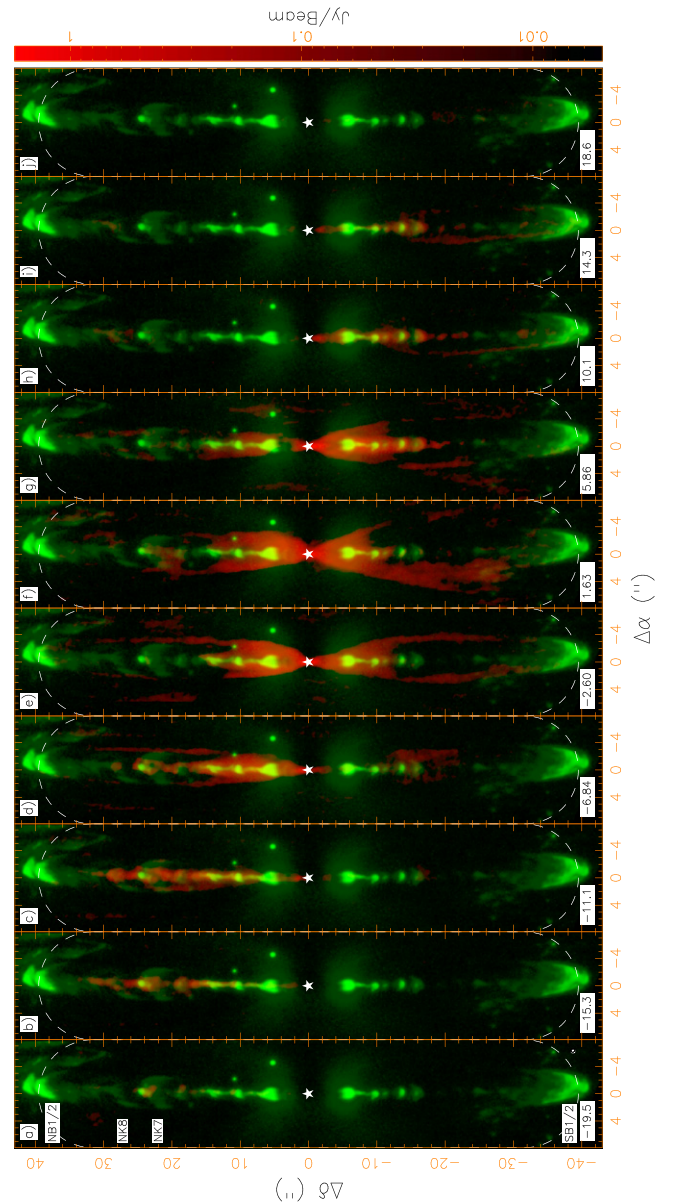


Figure 1. CO channel maps (red; logarithmic scale) compared to the H_2 map (green; adopted from McCaughrean et al. 2002) of the HH 121 system. The star marks the central source position. The channel velocity is indicated in the lower left corner. The dashed arcs outline the primary beam coverage in our ALMA observations. The synthesized beam in the CO maps has a size of $0''.56 \times 0''.47$ with a PA $\sim 20^\circ$, as shown in the lower right corner in panel (a).

smaller knots closer to the source, forming narrow internal shells around them. These inner shells are better seen as we zoom in to the inner part at low velocities, as shown in Figure 3. For the prominent pair of knots, NK1 and SK1, where the shocks are strong, hollow internal shells are clearly seen connecting to them (Figures 3(b) and (d)), as seen earlier in Lee et al. (2007). In summary, nested shells are seen in CO connecting to the bow shocks and knots, driven by them.

3.2. Molecular Jet in SiO and CO

Figure 4 shows the maps of the SiO emission and high-velocity (HV) CO emission compared to the H_2 map. As compared to the previous SMA maps in Lee et al. (2007, 2008), the maps here are created using slightly larger

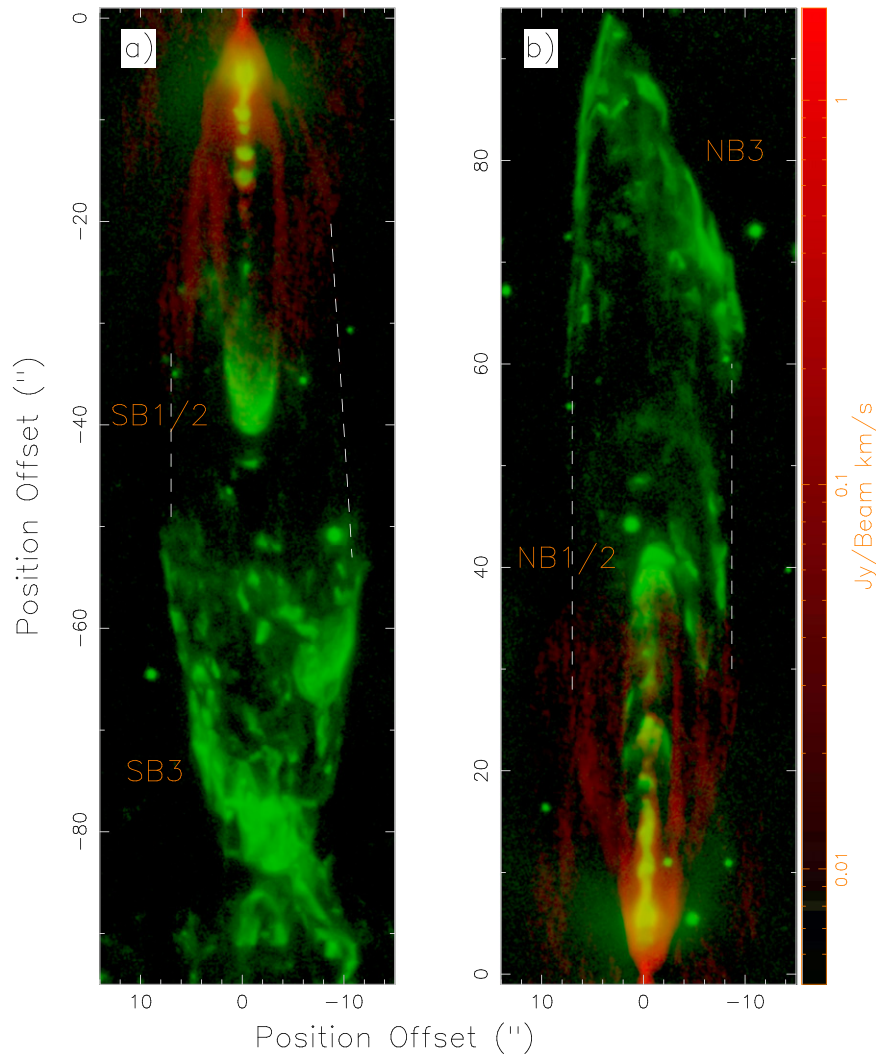


Figure 2. CO maps (red) integrated over selected velocity ranges that show the shell structures, compared to the H₂ map (green). In panel (a), the velocities are from -3.6 to -2.9 km s⁻¹, -2 to -1.3 km s⁻¹, 1.7 to 2.9 km s⁻¹, and 4.9 to 6.1 km s⁻¹. In panel (b), the velocities are from -7.8 to -5.6 km s⁻¹, -3.6 to 0.25 km s⁻¹, and 1.6 to 1.8 km s⁻¹. Nested CO shells are seen connecting to the H₂ bow shocks and knots. The dashed lines indicate the connections of the wide-opening shells to the big bow shocks, SB3 and NB3.

velocity ranges because ALMA detected the emission in slightly larger velocity ranges at a higher sensitivity. For the SiO map, we use the velocity from -23.03 to 17.53 km s⁻¹ instead of from -21.1 to 16 km s⁻¹. For the CO map, low-velocity emission is excluded to avoid the shell contamination. On the blueshifted side, we use the velocity from -21.65 to -8.95 km s⁻¹ instead of from -18.4 to -7.1 km s⁻¹. On the redshifted side, we use the velocity from 9.56 – 18.77 km s⁻¹ instead of from 3.4 – 13.3 km s⁻¹. Note that the high-velocity ranges are not symmetric with respect to the systemic velocity because the jet has a higher mean velocity and a larger velocity range on the blueshifted side than on the redshifted side (see Figure 5 in Lee et al. 2007), probably due to different inclination angles of the jet in the northern and southern parts (Lee et al. 2007). As found in Lee et al. (2007, 2008), both SiO and HV CO emissions trace the jet well, arising from the sinuous structures and knots in the jet seen in H₂. Note that since the H₂ map was made earlier, the SiO and CO emission peaks are seen slightly ahead of the H₂ emission peaks. As discussed in Lee et al. (2007), the jet has a slight bending of

$\sim 1^\circ.5$ to the west and a small semi-periodical wiggle in the trajectory.

Due to the higher sensitivity of ALMA, SiO emission becomes better detected toward the central source position, as compared to that seen in Lee et al. (2008), likely arising from the jet base near the source as seen in the lower transition line of SiO at $J = 5 - 4$ (Codella et al. 2007). Also, the jet appears to be more continuous in CO, especially in the northern part. In addition, three more knots were detected along the jet axis in the south, where no clear H₂ knot was detected. One knot was detected in SiO and CO between knots SK5 and SK7, and is thus labeled as knot SK6, as a counterpart of knot NK6 in the north. Two knots were detected in CO between knots SK6 and SK7, linking the two knots. The H₂ and CO emission seen between NK6 and NK7 could be their counterparts in the north. For the prominent knot SK1 where the shock is strong, the SiO emission is seen only at the bow tip, while the CO emission is seen mainly in the bow shock wings. The limb-brightened bow wing structure of the CO emission can be seen at lower velocities (Figure 3(d)). Similar morphology is also seen in L1157 in Gueth et al. (1998), probably because

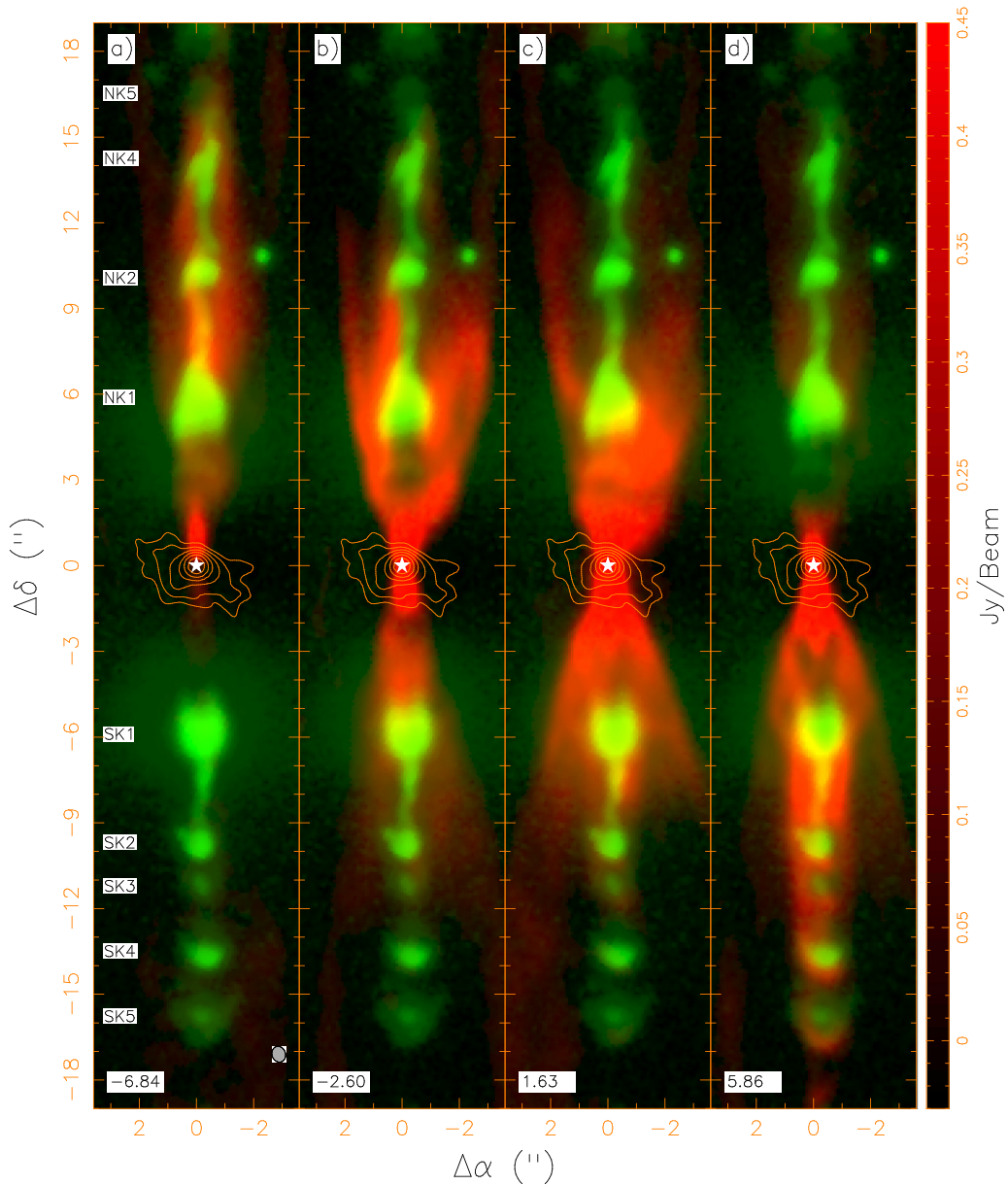


Figure 3. CO channel maps (red; linear scale) compared to the H_2 map of the HH 212 system in the inner part. The synthesized beam in the CO maps has a size of $0''.56 \times 0''.47$, as indicated in the lower right corner in panel (a). The star marks the central source position. The channel velocity is indicated in the lower left corner. The contours show the continuum map at 350 GHz adopted from Lee et al. (2014).

CO is destroyed or excited to higher transition lines at the tip where the shock is stronger.

The jet can also be seen at lower velocities (see Figure 1) because of the low inclination angle of the jet to the plane of the sky. Interestingly, at a higher angular resolution and sensitivity, the CO emission at 5.86 km s^{-1} appears to show a helical structure along the jet axis in the south (see Figure 3(d)) that was not seen before. This helical structure actually consists of a chain of small and similar-size bow shocks curving back to the jet axis, associated with the knots (SK2, SK3, SK4, and SK5) in the jet. The bow wings are faint in the west, causing them to appear as a helical structure. In addition, a faint jet-like structure can also be seen along the jet axis in between knots SK3 and SK4 at this velocity, tracing the jet itself. SiO emission also shows the similar bow shocks curving back to the jet axis (see Figure 4(b)). This feature has

been seen in the simulations of a pulsed jet, both unmagnetized (Stone & Norman 1993; Biro & Raga 1994; Völker et al. 1999) and magnetized (Stone & Hardee 2000). On the other hand, a pulsed wide-angle wind would produce a chain of wide bow shocks that do not curve back to the jet axis (Lee et al. 2001), inconsistent with our observations.

3.3. Proper Motion

Since the knots in the jet are well traced by the SiO emission, proper motion of the jet can be estimated by measuring the position shifts of their SiO emission peaks with respect to those seen ~ 6 yr earlier in our previous SMA map in Lee et al. (2008). We first convolved our previous SMA SiO map to the resolution of our ALMA map and then aligned the two maps with the continuum peaks. As shown in Figure 5, the jet pattern is similar in the two epochs, in agreement with the pattern

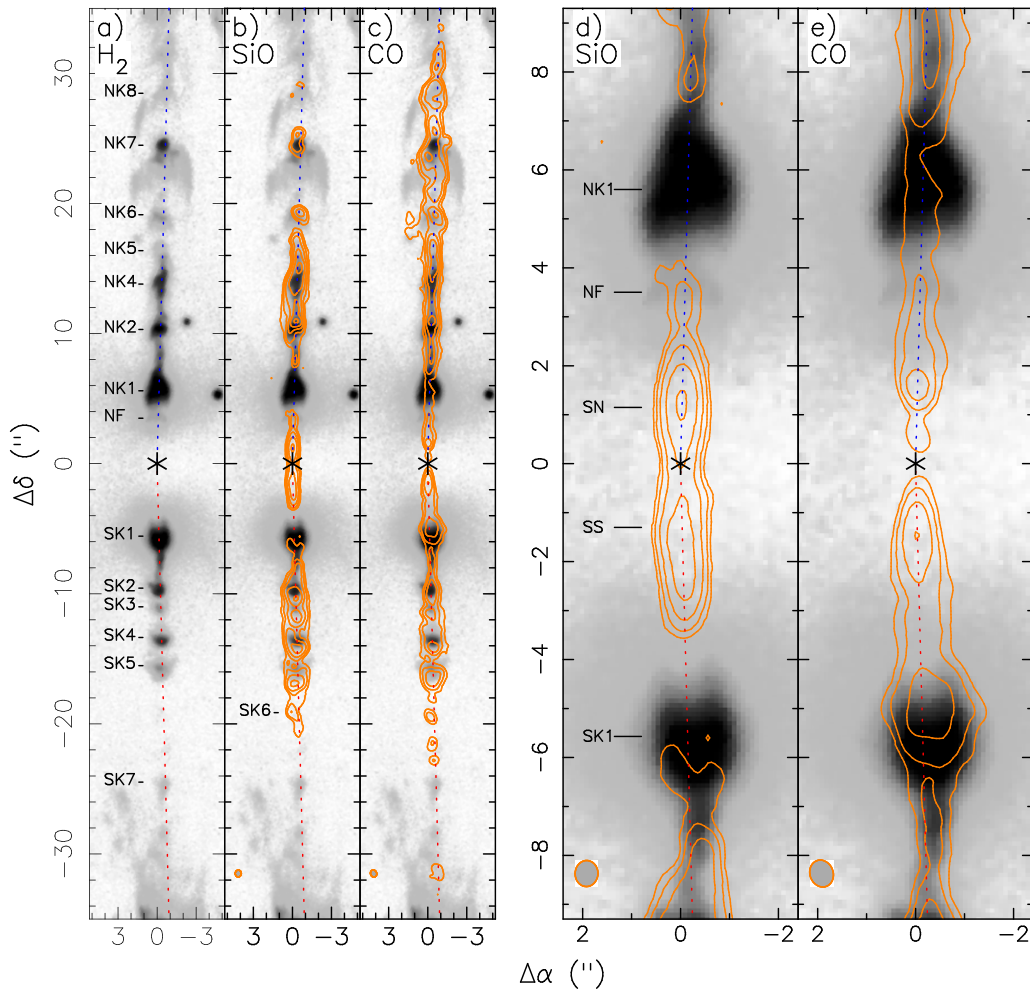


Figure 4. Jet in SiO, CO, and H₂. Gray image shows the H₂ map. In panel (b), contours show the SiO map (integrated from -23.03 to 17.53 km s⁻¹). Contour levels are $0.23 \times 2.5^{n-1}$ Jy beam⁻¹ km s⁻¹, where $n = 1, 2, 3 \dots$. In panel (c), contours show the high-velocity CO map (integrated from -21.65 to -8.95 km s⁻¹ on the blueshifted side and from 9.56 to 18.77 km s⁻¹ on the redshifted side). Contour levels are $0.20 \times 2^{n-1}$ Jy beam⁻¹ km s⁻¹, where $n = 1, 2, 3 \dots$. Panels (d) and (e) are the zoomed-in versions of panels (b) and (c), respectively.

propagating with the jet velocity. Only the knots that are resolved and have well-defined peaks are used for the measurement, with their emission peak positions marked with the solid lines. The innermost pair of knots, SS and SN, are not used for the measurement because they are spatially unresolved in our ALMA observations, appearing as jet-like structures. Thus, the mean position shift is estimated to be $\sim 0''.36 \pm 0''.15$. Hence, the proper motion is estimated to be $\sim 0''.06 \pm 0''.025$ yr⁻¹, giving rise to a tangential velocity of $\sim 115 \pm 50$ km s⁻¹. Since the jet is almost in the plane of the sky, the jet velocity can be approximated to this tangential velocity.

3.4. Jet Density and Mass-loss Rate

With a jet velocity better estimated and a CO emission better resolved than those reported in Lee et al. (2007), we can refine the jet density, and thus the mass-loss rate. The CO emission of the jet between knots NK1 and NK5 appears continuous and smooth (see Figure 4(c)), and thus can be used to derive the mean jet density. The mean CO intensity there is found to be ~ 1.2 Jy beam⁻¹ km s⁻¹. As discussed in Lee et al. (2007), the mean excitation temperature of the CO emission can be assumed to be ~ 50 K. Since the brightness temperature in the jet is mostly $\lesssim 20$ K, the CO emission can be assumed to

be optically thin. Assuming LTE, the column density of CO is estimated to be $\sim 2.3 \times 10^{16}$ cm⁻². The mean jet (H₂ volume) density can be derived from the CO column density using the conversion equation, e.g., Equation (17) in Lee et al. (2014). With a CO abundance of 8.5×10^{-5} and a jet diameter of $\sim 0''.2$ (Cabrit et al. 2007; Lee et al. 2008), the mean jet density is estimated to be $\sim 5.6 \times 10^5$ cm⁻³, similar to the mean value derived from HCO⁺ in Lee et al. (2014). Thus, the (two-sided) mass-loss rate would be $\dot{M}_j \sim 1.1 \times 10^{-6} M_\odot$ yr⁻¹. Since the accretion rate has been estimated to be $\sim 5 \times 10^{-6} M_\odot$ yr⁻¹ (Lee et al. 2014), the mass-loss rate is estimated to be $\sim 20\%$ of the accretion rate, reasonably consistent with the X-wind model ($\sim 30\%$; Shu et al. 2000) and the disk-wind model ($\sim 10\%$; Konigl & Pudritz 2000).

4. DISCUSSION

4.1. Bow Shock Formation and Sideways Ejection

As was discussed earlier, the knots in the southern jet are seen with small bow shocks, with their bow wings curving back to the jet axis. Knots SK4 and SK5 are reasonably resolved, allowing us to study the formation mechanism of the bow shocks. For knot SK5, the CO emission peak appears

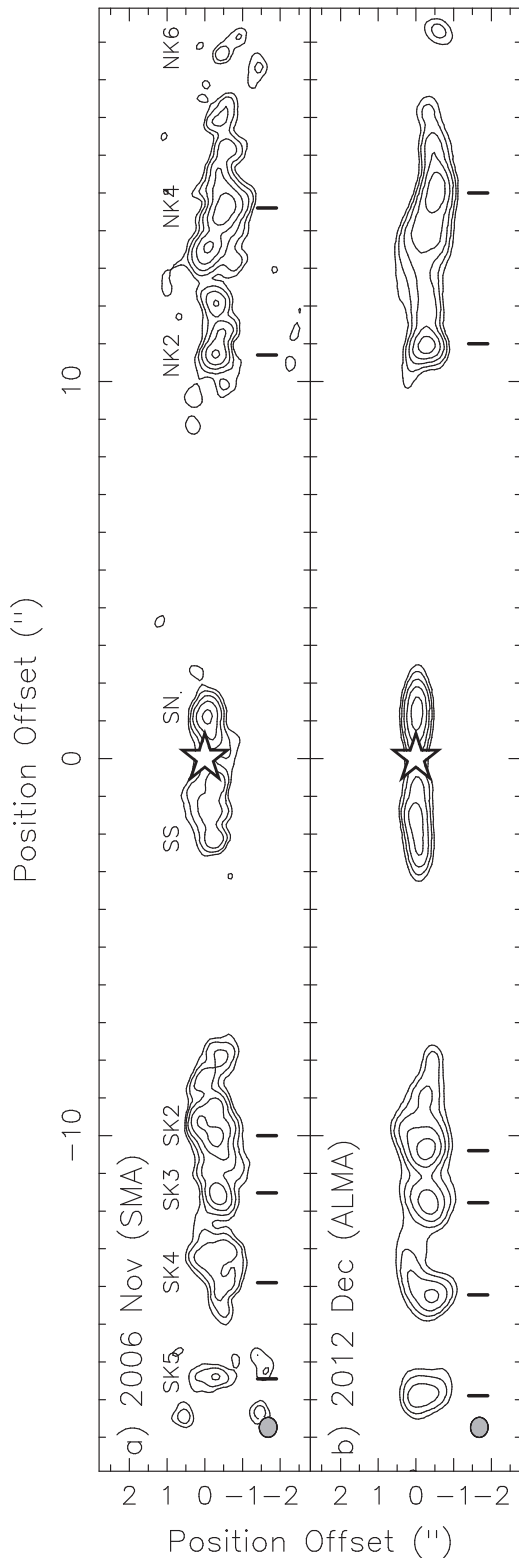


Figure 5. Proper motion measurement using the SiO knots in the jet in two different epochs with an ALMA angular resolution of $0''.56 \times 0''.47$. Contour levels are $1.2 \times 1.6^{n-1} \text{ Jy beam}^{-1} \text{ km s}^{-1}$, where $n = 1, 2, 3 \dots$. The star marks the central source position. The line segments indicate the SiO peak positions of the knots.

clearly upstream of (i.e., closer to the central source than) the SiO emission peak (Figure 6(a)). For knot SK4, the CO emission peak appears only slightly upstream of the SiO emission peak by $0''.08$ or $\sim 15\%$ of the beam size, thus higher

resolution observations are needed to confirm it. In SiO, the position–velocity (PV) diagram cut along the jet axis shows an arc-like PV structure for each knot with an apex at the velocity of $\sim 9 \text{ km s}^{-1}$ pointing away from the source, as shown in Figure 6(b). As we move away from the apex, either to higher velocity or to lower velocities, the PV structure bends slightly toward the source direction, forming the arc-like PV structure. The CO emission shows a similar PV structure slightly upstream of that of the SiO emission. Note that the CO emission is missing from ~ 8 to 10 km s^{-1} due to a foreground cloud at those velocities. In the northern jet, the knots are not spatially resolved and thus no clear bow-like structures can be seen in SiO and CO. Higher resolution observations are needed to study them.

Arc-like PV structures have been seen in pulsed jet simulations (see e.g., Figure 16(a) in Stone & Norman 1993). In those simulations, even though the jet source is continuously ejecting material with a constant density, a (sinusoidal) variation in the ejection velocity produces an internal working surface (IWS) in the jet (Biro & Raga 1994). The IWS can appear as a small arc-like knot, with its velocity increasing toward its two edges from the jet axis (see Figure 7, and also Figure 10 in Lee & Sahai 2004), producing the arc-like PV structure. As its shocked material is ejected sideways into the outflow cavity, it forms a bow shock, with the bow wings curving back to the jet axis (Biro & Raga 1994), like those of knots SK4 and SK5 (see Section 3.2). Therefore, knots SK4 and SK5 likely trace the IWSs in the jet. A bigger variation in the jet velocity would produce a faster and more massive sideways ejection, forming stronger bow shocks (Raga et al. 2002), such as SK1, NK1, NB1/2, and SB1/2, and thus bigger internal shells extending backward to the central source from their bow wings, as seen in the pulsed jet simulations in Biro & Raga (1994) and Lee et al. (2001).

Sideways ejection has been claimed in another jet source IRAS 04166+2706 (Santiago-García et al. 2009). In that jet, a sawtooth pattern was seen in the PV diagram cut along the jet axis in CO and SiO, and it was argued to be produced by the sideways ejection of the shocked material in the IWSs. That jet is highly inclined, with an inclination angle of $\sim 45^\circ$ to the plane of the sky. Viewing the IWSs at a high inclination angle produces the sawtooth PV pattern, as predicted in the simulated PV diagram at a high inclination angle in Stone & Norman (1993). Here the HH 212 jet is almost in the plane of the sky with a small inclination angle, thus the sideways ejection forms the arc-like PV structures in the PV diagram.

4.2. Wide-angle Wind Component?

In addition to a collimated jet, an unseen wide-angle wind seems to be needed in driving molecular outflows in the later stage of star formation (Lee & Ho 2005; Arce et al. 2013). Is a wide-angle wind also needed in the early phase of star formation as in HH 212? Recently, a wide-angle flow has been seen in C^{34}S and may suggest the presence of a wide-angle wind (Codella et al. 2014). This wide-angle flow has also been seen earlier in HCO^+ (Lee et al. 2014) and it may trace the cavity walls instead. In addition, a wide-angle wind, if it exists, would produce wide bow shocks, and thus wide internal shells (Lee et al. 2001). This is inconsistent with our observations, which show highly curved bow shocks and narrow shells driven by the knots. Therefore, in this source, the wide-angle wind, if it exists, is not significant enough to affect the structures of the bow shocks and the shells. This is not

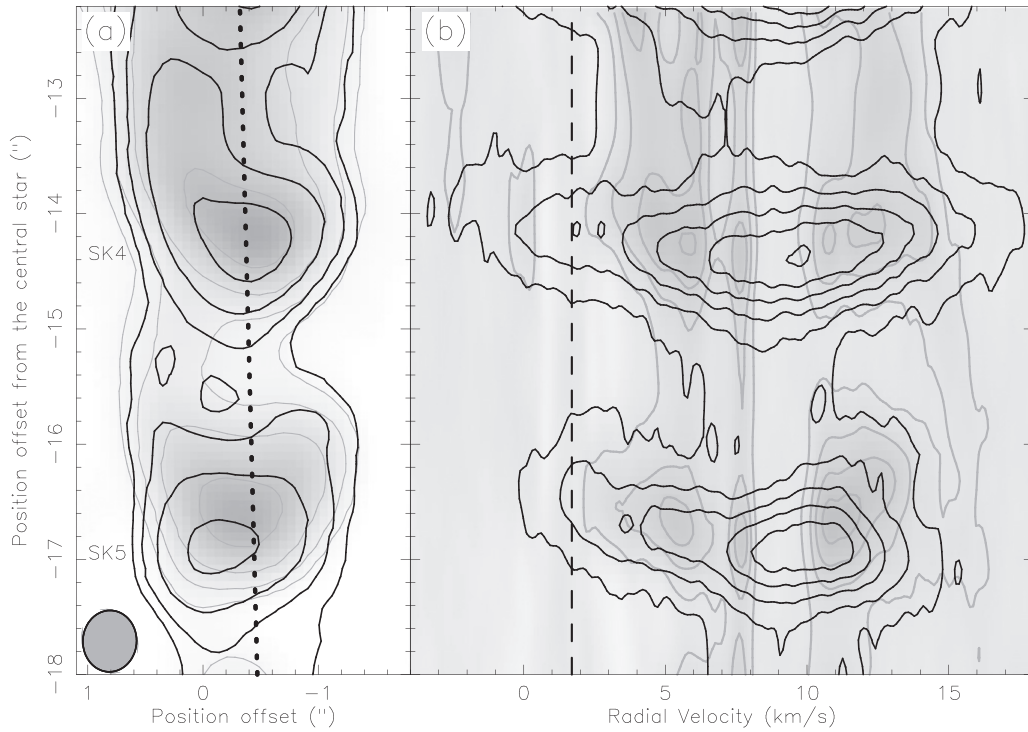


Figure 6. Structure and kinematics of knots SK4 and SK5 in the south. Gray contours in the image are for CO and black contours are for SiO. (a) The SiO map is the same as in Figure 4, but zooming into knots SK4 and SK5, highlighting their bow-like structures. The CO map shows the total CO emission of knots SK4 and SK5 integrated from 2.2 to 15.4 km s⁻¹. Contour levels are $0.25 \times 2^{n-1}$ Jy beam⁻¹ km s⁻¹, where $n = 1, 2, 3 \dots$. The dotted line indicates the jet axis in the south. (b) Position–velocity (PV) diagrams cut along the jet axis for knots SK4 and SK5. The vertical dashed line indicates the systemic velocity of 1.7 km s⁻¹. The contour levels start at 40 mJy beam⁻¹ with a step of 160 mJy beam⁻¹ for CO, and start at 30 mJy beam⁻¹ with a step of 120 mJy beam⁻¹ for SiO.

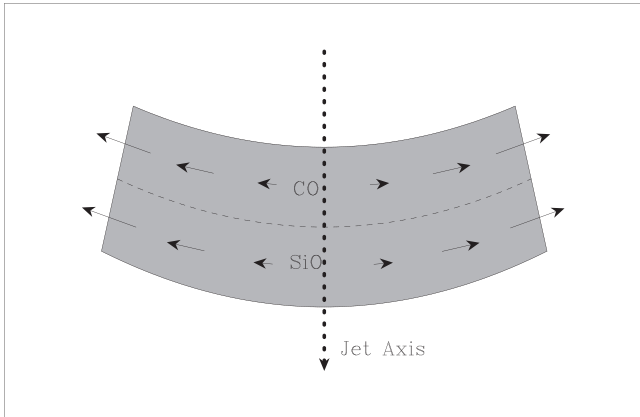


Figure 7. Velocity structure of the shocked material in an internal working surface (IWS) in the shock frame moving down the jet axis. The vectors show the material motion, with the length showing the magnitude. Two layers, CO and SiO, are plotted as an illustration based on our observational results.

inconsistent with current jet launching models (Konigl & Pudritz 2000; Shu et al. 2000), which predict a wide-angle wind much more tenuous, and thus less significant, than the central jet. In the later phase, the jet is much more tenuous so the contribution of the wide-angle wind could become more important (Lee & Ho 2005; Arce et al. 2013).

4.3. Jet Wiggle

The jet wiggle can be better seen after combining the CO and SiO maps of ALMA with the H₂ map, as shown in Figure 8. The northern jet is continuous and the wiggle is reasonably well defined. The southern jet appears to be continuous only up

to knot SK2 at $\sim -10''$, and thus the wiggle is not so well defined. Comparing the sinuous structures between knots SK1 and SK2 to those between knots NK1 and NK2, the wiggle in the southern jet could be roughly point symmetric to that in the northern jet. Therefore, we first model the wiggle in the northern jet and then apply the model to the southern jet assuming a point symmetric wiggle about the central source.

A possible mechanism to produce a point-symmetric wiggle is the jet precession (Raga et al. 2009). In this case, the amplitude of the wiggle, A , will increase linearly with the distance, i.e.,

$$A(z) = z \tan \theta_0 \quad (1)$$

where z measures the distance of the jet from the source along the jet axis. Here θ_0 is the half-opening angle of the wiggle, so that $\tan \theta_0$ gives the rate of the growth in the amplitude with the distance. The wiggle appears to be semi-periodical and thus can be assumed to be given by the following sinusoidal model

$$x(z) = A(z) \sin \left(\frac{2\pi z}{\lambda} + \phi_0 \right) \quad (2)$$

where x measures the displacement of the jet perpendicular to the jet axis. λ is the wavelength of the wiggle and ϕ_0 is the phase angle at the source. Based on the wiggle of the northern jet, the best parameters are $\theta_0 \sim 0.5^\circ \pm 0.2^\circ$, $\lambda \sim 5''.6 \pm 1''.0$ (or 2240 ± 400 AU), and $\phi_0 \sim 0^\circ \pm 50^\circ$. Since the jet velocity is ~ 115 km s⁻¹, the period of the wiggle is ~ 93 yr. As seen in Figure 8(a), the model can roughly reproduce the wiggle of both the northern and southern jet in the inner part, but seems to predict a larger wiggle than the observed in the outer part with $|z| \gtrsim 20''$.

In order to improve the model, the amplitude of the wiggle is assumed to first increase linearly with the distance and then

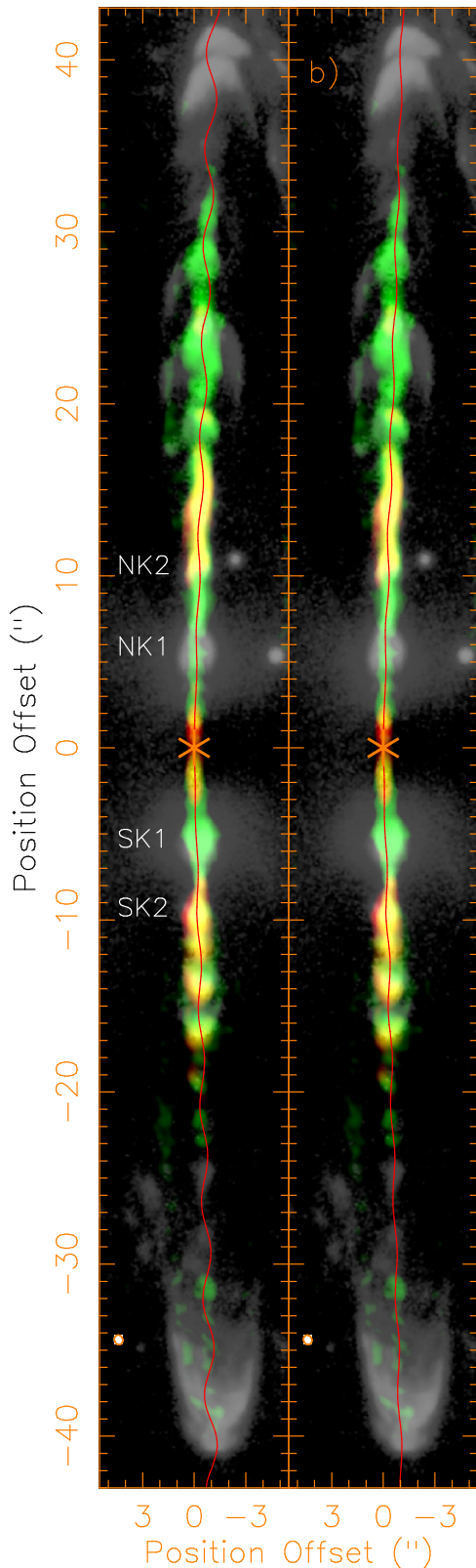


Figure 8. Wiggle of the jet and the model for the wiggle (red curves). The gray image is H_2 , green image is high-velocity CO, and red image is SiO, all from Figure 4. (a) The model assumes a constant growth in the wiggle amplitude with the distance from the central source. (b) A revised model assumes a constant wiggle amplitude for a distance greater than $10''$ from the central source.

remain constant at $z \geq z_0$, i.e.,

$$A(z) = \begin{cases} z \tan \theta_0 & \text{if } z < z_0, \\ z_0 \tan \theta_0 & \text{if } z \geq z_0 \end{cases} \quad (3)$$

As shown in Figure 8(b), the model with $z_0 \sim 10''$ (4000 AU) can give a better match up to $\sim 34''$ (i.e., 6 cycles of wiggle) in the northern jet and up to $\sim 38''$ in the southern jet, where the SiO and CO emission were detected. At $z = z_0$, the amplitude of the wiggle reaches the maximum value of $A_m \equiv z_0 \tan \theta_0 \sim 0''.1$, roughly the same as the jet radius, which is also $\sim 0''.1$ (Cabrit et al. 2007; Lee et al. 2008). Note that, since the southern jet does not have a continuous structure beyond $\sim 10''$ from the source, further observations are still needed to confirm that the wiggle of the jet is really point symmetric about the central source. Observations at higher angular resolutions are also needed to refine the value of z_0 .

If the wiggle is really point symmetric about the central source, then one way to produce the wiggle is from the jet precession due to the tidal interaction of a binary companion on the disk of the jet source (Terquem et al. 1999). However, if this is the case, the amplitude of the wiggle is expected to grow with the distance (Raga et al. 2009), which is inconsistent with our observations.

Another possibility is the current-driven kink instability (Cerqueira & de Gouveia Dal Pino 2001), since the jet is expected to be magnetized with a helical magnetic field morphology (Konigl & Pudritz 2000; Shu et al. 2000). In this case, the amplitude of the wiggle is expected to grow at the beginning and then become saturated and thus remain roughly constant at large distances; see, e.g. Figure 3 in both Cerqueira & de Gouveia Dal Pino (2001) and Mizuno et al. (2014). In addition, the wiggle is more like an oscillation, and thus could be semi-periodical. Both of these are roughly consistent with what we observe here in our jet. However, the wiggle is not expected to show any symmetry about the central source. This might be OK because the jet wiggle here may not be point symmetric, as was mentioned earlier. In addition, the detailed jet structure here already appears to be different between the northern and southern jets. For the kink instability to take place, we have the Kruskal–Shafranov criterion $|B_p/B_\phi| < \lambda/2\pi A_m$ (e.g., Bateman 1978). With the maximum displacement $A_m \sim 0''.1$ and the wiggle wavelength $\lambda \sim 5''.6$, we have $|B_p/B_\phi| < 9$. Therefore, this kink instability, if in action, could be initiated in the central part of the jet where the magnetic field is dominated by the poloidal field (Pudritz et al. 2012). This poloidal field could serve a “backbone” to stabilize the jet (Ouyed et al. 2003). The toroidal field dominates only near the jet edges in order to collimate the jet.

5. CONCLUSIONS

We have mapped the HH 212 jet and outflow system in the SiO ($J = 8 - 7$) and CO ($J = 3 - 2$) lines. Our primary conclusions are the following.

1. Although the jet is seen with knots and bow shocks, the underlying jet is continuous, especially in the northern side.

2. The proper motion of the jet is estimated to be $\sim 115 \pm 50$ km s⁻¹. The mass-loss rate in the jet is refined to be $\sim 1.1 \times 10^{-6} M_{\odot} \text{ yr}^{-1}$, as expected for a Class 0 source.
3. Some knots are seen associated with small bow shocks, with their bow wings curving back to the jet axis. Two of them, e.g., knots SK4 and SK5, are reasonably resolved, showing kinematics consistent with a sideways ejection, likely tracing the IWSs formed in a collimated jet due to a temporal variation in the jet velocity. Their bow shocks are formed by this sideways ejection.
4. The jet has a small semi-periodical wiggle, with a period of ~ 93 yr. The amplitude of the wiggle first increases with the distance and then stays roughly constant. A jet precession may have difficulty explaining this kind of wiggle. One possible origin of the wiggle could be the kink instability in a magnetized jet.
5. Nested (internal) shells are seen in CO connecting to the knots and bow shocks driven by them. The sideways ejection ejects material into the outflow cavity from the knots, forming the bow shocks and the internal shells.
6. The internal shells of the knots are narrow and the bow shocks of the knots curve back to the jet axis, both suggesting that the wide-angle wind, if it exists, is insignificant compared to the jet.

We thank the anonymous referee for insightful comments. This paper makes use of the following ALMA data: ADS/JAO. ALMA#2011.0.00647.S. ALMA is a partnership of the ESO (representing its member states), NSF (USA), and NINS (Japan) together with the NRC (Canada) and NSC and ASIAA (Taiwan), in cooperation with the Republic of Chile. The Joint ALMA Observatory is operated by the ESO, AUI/NRAO, and NAOJ. These data were made available to C.-F.L. as part of his ALMA proposal 2011.0.00122.S (PI: Chin-Fei Lee), which requested observations duplicating those of proposal 2011.0.00647.S. C.-F.L. acknowledges grants from the National Science Council of Taiwan (NSC 101-2119-M-001-002-MY3) and the Academia Sinica (Career Development Award).

REFERENCES

- Arce, H. G., Mardones, D., Corder, S. A., et al. 2013, *ApJ*, **774**, 39
- Bateman, G. 1978, *MHD Instabilities* (Cambridge, MA: MIT Press)
- Biro, S., & Raga, A. C. 1994, *ApJ*, **434**, 221
- Cabrit, S., Codella, C., Gueth, F., et al. 2007, *A&A*, **468**, L29
- Carrasco-González, C., Rodríguez, L. F., Anglada, G., et al. 2010, *Sci*, **330**, 1209
- Cerqueira, A. H., & de Gouveia Dal Pino, E. M. 2001, *ApJ*, **560**, 779
- Claussen, M. J., Marvel, K. B., Wootten, A., & Wilking, B. A. 1998, *ApJL*, **507**, L79
- Codella, C., Cabrit, S., Gueth, F., et al. 2007, *A&A*, **462**, L53
- Codella, C., Cabrit, S., Gueth, F., et al. 2014, *A&A*, **568**, L5
- Coffey, D., Bacciotti, F., Chrysostomou, A., Nisini, B., & Davis, C. 2011, *A&A*, **526**, AA40
- Frank, A., Ray, T. P., Cabrit, S., et al. 2014, arXiv:1402.3553
- Gueth, F., Guilloteau, S., & Bachiller, R. 1998, *A&A*, **333**, 287
- Königl, A., & Pudritz, R. E. 2000, *Protostars and Planets IV*, ed. V. Mannings, A. P. Boss, & S. S. Russell (Tucson, AZ: Univ. Arizona Press), 759
- Lee, C., & Ho, P. T. P. 2005, *ApJ*, **624**, 841
- Lee, C.-F., Hirano, N., Zhang, Q., et al. 2014, *ApJ*, **786**, 114
- Lee, C.-F., Ho, P. T. P., Beuther, H., et al. 2006, *ApJ*, **639**, 292
- Lee, C.-F., Ho, P. T. P., Bourke, T. L., et al. 2008, *ApJ*, **685**, 1026
- Lee, C.-F., Ho, P. T. P., Hirano, N., et al. 2007, *ApJ*, **659**, 499
- Lee, C.-F., Mundy, L. G., Reipurth, B., Ostriker, E. C., & Stone, J. M. 2000, *ApJ*, **542**, 925
- Lee, C.-F., Rao, R., Ching, T.-C., et al. 2014b, *ApJL*, **797**, LL9
- Lee, C.-F., & Sahai, R. 2004, *ApJ*, **606**, 483
- Lee, C.-F., Stone, J. M., Ostriker, E. C., & Mundy, L. G. 2001, *ApJ*, **557**, 429
- McCaughrean, M., Zinnecker, H., Andersen, M., Meeus, G., & Lodieu, N. 2002, *Msngr*, **109**, 28
- Mizuno, Y., Hardee, P. E., & Nishikawa, K.-I. 2014, *ApJ*, **784**, 167
- Ouyed, R., Clarke, D. A., & Pudritz, R. E. 2003, *ApJ*, **582**, 292
- Pudritz, R. E., Hardcastle, M. J., & Gabuzda, D. C. 2012, *SSRv*, **169**, 27
- Raga, A. C., Esquivel, A., Velázquez, P. F., et al. 2009, *ApJL*, **707**, L6
- Raga, A. C., Velázquez, P. F., Cantó, J., & Masciadri, E. 2002, *A&A*, **395**, 647
- Santiago-García, J., Tafalla, M., Johnstone, D., & Bachiller, R. 2009, *A&A*, **495**, 169
- Shu, F. H., Najita, J. R., Shang, H., & Li, Z.-Y. 2000, *Protostars and Planets IV*, ed. V. Mannings, A. P. Boss, & S. S. Russell (Tucson, AZ: Univ. Arizona Press), 789
- Stone, J. M., & Hardee, P. E. 2000, *ApJ*, **540**, 192
- Stone, J. M., & Norman, M. L. 1993, *ApJ*, **413**, 210
- Terquem, C., Eisloffel, J., Papaloizou, J. C. B., & Nelson, R. P. 1999, *ApJL*, **512**, L131
- Völker, R., Smith, M. D., Suttner, G., & Yorke, H. W. 1999, *A&A*, **343**, 953
- Zinnecker, H., McCaughrean, M. J., & Rayner, J. T. 1998, *Natur*, **394**, 862